Newton

Article

# Colloidal Magnus effect in polymer solutions

## Graphical abstract

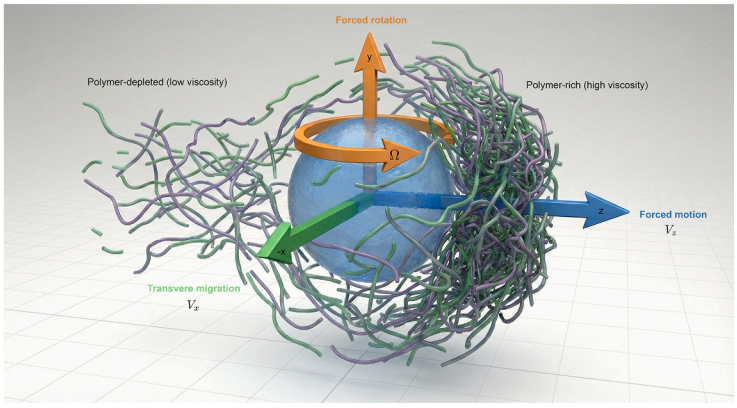


## Highlights

- Microstructural origin of inverse Magnus effect of colloids is identified
- Colloidal migration is driven by polymer density inhomogeneities (dipole)
- Stress relaxation, normal-stress, and shear-thinning mechanisms are ruled out
- Theory predicts experiment observations without fitting parameters

## Authors

Marco De Corato, Kun Zhang, Lailai Zhu

## Correspondence

mdecorato@unizar.es (M.D.C.),
lailai_zhu@nus.edu.sg (L.Z.)

## In brief

Toward elucidating the microscopic origin of the Magnus effect, De Corato et al. theoretically identify and validate polymer transport induced by stress gradient, which causes unexpected sideways drifts of colloids in complex fluids. This understanding facilitates the prediction of colloidal motion and guides the design of microscale devices operating in complex fluid environments. Achieving parameter-free agreement with recent experiments confirms the physical insights underlying the theory.

De Corato et al., 2026, Newton *2*, 100373
May 4, 2026 © 2025 The Author(s). Published by Elsevier Inc.
https://doi.org/10.1016/j.newton.2025.100373

CellPress

Please cite this article in press as: De Corato et al., Colloidal Magnus effect in polymer solutions, Newton (2025), https://doi.org/10.1016/j.newton.2025.100373

Newton

CellPress
OPEN ACCESS

Article

# Colloidal Magnus effect in polymer solutions

Marco De Corato,[1,*] Kun Zhang,[2] and Lailai Zhu[2,3,*]
[1]Aragon Institute of Engineering Research (I3A), University of Zaragoza, Zaragoza, Spain
[2]Department of Mechanical Engineering, National University of Singapore, Singapore, Singapore
[3]Lead contact
*Correspondence: mdecorato@unizar.es (M.D.C.), lailai_zhu@nus.edu.sg (L.Z.)
https://doi.org/10.1016/j.newton.2025.100373

**ACCESSIBLE OVERVIEW** For decades, the transverse migration of rotating particles—known as the Magnus effect—has been understood through the lens of fluid inertia, a mechanism irrelevant at the low Reynolds numbers of colloidal systems. The discovery of an inverse Magnus effect for colloids in viscoelastic polymer solutions challenged this classical understanding, prompting explanations based on the fluid's memory and nonlinear stress features. We present a theoretical and numerical investigation that revises the mechanism driving this low-Reynolds-number phenomenon. Our findings rule out conventional viscoelastic properties, such as stress relaxation and normal-stress differences, as the main cause of the inverse colloidal migration. Instead, we identify a distinct, microstructural mechanism: the inverse Magnus effect originates from local polymer density inhomogeneities. The particle's translation generates gradients in the fluid stress, which in turn drive the transport of polymers, leading to a dipolar distribution of polymer concentration and local viscosity around the colloid. This non-uniform viscosity profile then couples with the particle's rotation to produce the transverse migration force. Incorporating this stress-gradient-induced polymer transport into our model yields a simple, mechanistic theory that quantitatively predicts experimental data without fitting parameters, confirming the identified mechanism. This work establishes stress-gradient-induced polymer transport as an indispensable mechanism for accurately modeling microscopic objects in complex fluids, with direct implications for future designs of microfluidics and micro-machinery.

## SUMMARY

Rotating particles moving in fluids undergo a transverse migration via the inertia-induced Magnus effect. This phenomenon vanishes at colloidal scales because inertia is negligible and the fluid flow is time reversible. Yet, recent experiments discovered an inverse Magnus effect of colloids in polymeric and micellar solutions, supposedly because their viscoelasticity breaks the time reversibility. Our study shows that classical viscoelastic features—stress relaxation, normal-stress differences, and/or shear thinning—cannot explain this phenomenon. Instead, it originates from local polymer density inhomogeneities due to their stress-gradient-induced transport, a mechanism increasingly important at smaller scales—indeed, relevant to colloidal experiments. Incorporating this mechanism into our model leads to quantitative agreement with the experiments without fitting parameters. Our work provides new insights into colloidal motion in complex fluids with microstructural inhomogeneities, offers a simple mechanistic theory for predicting the resulting migration, and underscores the necessity of assimilating these findings in future designs of micro-machinery, such as those including swimmers, actuators, or rheometers.

## INTRODUCTION

The viscoelasticity of polymeric fluids enables them to exhibit effects that are often distinct or even contrary to those triggered by weak or intermediate inertia in Newtonian fluids. Consider a macroscopic object forced to move in water; if the force is removed suddenly, it continues to cruise forward due to inertia. Conversely, a colloid in viscoelastic fluids moves backward upon force removal—a phenomenon termed recoil in microrheology.[1] Another example is the rod-climbing or "Weissenberg" effect,[2] where the free surface of a complex fluid climbs up a spinning rod, whereas the near-rod surface would bend down in Newtonian fluids with inertia. Similarly, while inertia drives the wind from the poles to the equator at the scale of the rotating Earth, desktop experiments[3,4] showcased a reversely directed secondary flow around a rotating sphere in polymeric liquids.

Recent experiments[5] presented another compelling illustration of this contrasting trend. A spinning and translating


This is an open access article under the CC BY license (http://creativecommons.org/licenses/by/4.0/).

Please cite this article in press as: De Corato et al., Colloidal Magnus effect in polymer solutions, Newton (2025), https://doi.org/10.1016/j.newton.2025.100373



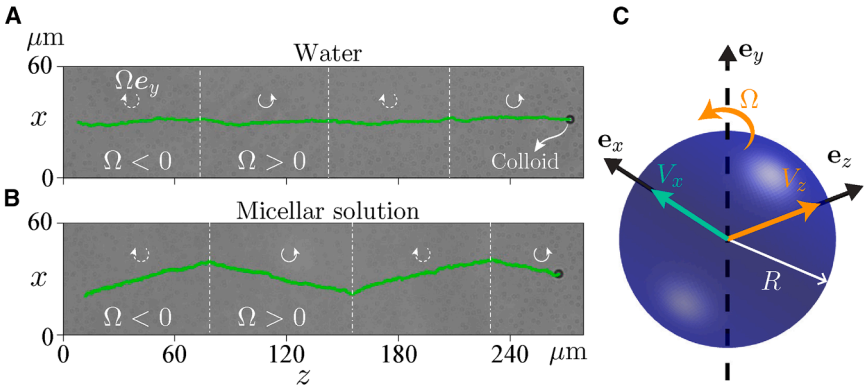


**Figure 1. Experimental observations motivating this study and schematic illustration**

(A) Experiments demonstrate that a colloid spinning about $\mathbf{e}_y$ and translating along $\mathbf{e}_z$ in water exhibits negligible lateral ($\mathbf{e}_x$) motion. Green curves indicate the trajectories of colloids. Adapted from Cao et al.[5] under CC BY 4.0 (https://creativecommons.org/licenses/by/4.0/).

(B) Contrastingly, it experiences an inverse Magnus effect in a micellar solution. Adapted from Cao et al.[5] under CC BY 4.0 (https://creativecommons.org/licenses/by/4.0/).

(C) Schematic of our model showing a spherical particle of radius $R$ with a prescribed translational velocity $V_z$ and rotational velocity $V_x$, with its migration velocity $V_x$ to be determined.

micron-sized colloidal particle in micellar solutions with negligible inertia was observed migrating perpendicular to both its spinning and translational axes (see Figure 1B). Intriguingly, the transversal migration was oriented opposite to that observed in inertial Newtonian fluids—a phenomenon commonly known as the Magnus effect.[6,7] Such an inverse Magnus migration disappears when driving the colloid in a Newtonian fluid (see Figure 1A), as forbidden by the time reversibility of the Stokes flow.

In viscoelastic fluids, the combination of elastic memory effects and nonlinear normal stresses breaks the time reversibility, allowing micron-sized particles to migrate across streamlines within complex fluids. Since its first observation by Karnis and Mason,[8] particulate migration due to normal-stress differences has been widely reported.[9–15] Typically, such phenomena are associated with non-uniform shear rates and/or geometric asymmetries, as exemplified by the lateral motion of particles toward the centerline of a Poiseuille flow and the outer wall of a rotating Couette flow.[9,10,16] These findings have spurred research into viscoelastic microfluidics for particle manipulation[13,14,17–28] and material property measurements.[29] Another example is the horizontal drift of a sedimenting colloid along the flow or gradient direction of a shear flow,[30–32] driven by local variations in shear rate induced by the colloid's translation. Beyond these scenarios with an ambient flow, normal-stress imbalances owing to geometric asymmetry can enable spinning[33–35] or swinging[36] objects to propel in quiescent environments.

While normal stress differences could explain the transversal colloidal migration observed by Cao et al.,[5] the authors propose a simplified phenomenological model that attributes the migration to polymer concentration inhomogeneities instead. This argument leaves the precise mechanism underlying the Magnus effect unresolved. Clarifying this mechanism could unveil whether the effect is a generic feature of colloids that spin while translating through complex fluids.

To gain a definitive mechanistic insight, we elucidate the microscopic origin of the Magnus effect by theoretically and numerically solving the fluid flow and rheological constitutive equations. We find that relaxation dynamics, normal-stress differences, and/or shear thinning, typical of polymer solutions, cannot explain the Magnus migration. This finding contrasts with the abovementioned studies that typically link similar low-Reynolds-number colloidal migration in viscoelastic media to their normal-stress differences. Crucially, we identify, through asymptotic analysis and simulations, the flow-induced inhomogeneous distribution of polymers as an indispensable enabler for the new Magnus effect—a mechanism proposed phenomenologically by Cao et al.[5] Importantly, our asymptotic prediction of the Magnus effect quantitatively aligns with experimental data.[5]

## RESULTS

### Problem setup for spinning colloid under forced translation in a polymer solution

We consider a spherical particle of radius $R$ suspended in a polymer solution. The particle is centered within a co-moving Cartesian coordinate system (see Figure 1C). It rotates steadily around the $y$ axis with angular velocity $\Omega\mathbf{e}_y$ while simultaneously translating along the $z$ axis at a constant velocity $V_z$. Due to the Magnus effect, the particle might migrate transversely, i.e., in the $x$ direction. This corresponding transversal velocity $V_x$ remains to be determined as part of the solution.

By neglecting the particle and fluid inertia, the governing equations for the velocity $\mathbf{v}$ and pressure $p$ of the polymeric fluid flow are

$$\nabla\cdot\mathbf{v} = 0 \quad \text{and} \quad \nabla\cdot(2\eta_s\mathbf{E} - p\mathbf{I} + \boldsymbol{\tau}) = \mathbf{0}, \qquad \text{(Equation 1)}$$

where $\eta_s$ is the solvent viscosity, $\mathbf{E} = [\nabla\mathbf{v} + (\nabla\mathbf{v})^T]/2$ the strain-rate tensor, and $\boldsymbol{\tau}$ the polymeric stress. Far from the particle, the fluid velocity $\mathbf{v} = -V_z\mathbf{e}_z - V_x\mathbf{e}_x$. At the surface $\mathcal{S}$ of the particle, $\mathbf{v} = \Omega\mathbf{e}_y \times \mathbf{r}$, where $\mathbf{r}$ is the position vector. To determine the migration velocity $V_x$, we apply the force-free condition that the total hydrodynamic force exerted on the particle vanishes in the $x$ direction, namely, $\int_{\mathcal{S}}(2\eta_s\mathbf{E} - p\mathbf{I} + \boldsymbol{\tau}) : \mathbf{n}\mathbf{e}_x d\mathcal{S} = 0$, where $\mathbf{n}$ denotes the fluid-pointing unit normal.

### Unobserved Magnus migration in Oldroyd-B fluids

To model the polymeric fluid flow, we first attempt the widely employed Oldroyd-B (OB) constitutive equation,[37–39] which represents polymers as linear elastic dumbbells with a spring constant $k$. The polymers are homogeneously distributed in a Newtonian solvent, with a uniform number density $n = n_\infty$, where $n_\infty$ is the

Please cite this article in press as: De Corato et al., Colloidal Magnus effect in polymer solutions, Newton (2025), https://doi.org/10.1016/j.newton.2025.100373



CellPress
OPEN ACCESS

constant far-field density. The polymeric stress $\boldsymbol{\tau} = k\mathbf{C} - k_BTn\mathbf{I}$ scales linearly with the deviation of the density-weighted chain conformation, $\mathbf{C}$, from its thermal equilibrium. Here, $k_B$ indicates the Boltzmann constant, and $T$ is the absolute temperature. The governing equation for $\mathbf{C}$ is[40]

$$\lambda\overset{\nabla}{\mathbf{C}} + \mathbf{C} - \frac{k_BT}{k}n\mathbf{I} = \mathbf{0}, \qquad \text{(Equation 2)}$$

where $\lambda$ is the relaxation time of the polymers and the upper convected derivative is defined as $\overset{\nabla}{\mathbf{C}} = \frac{\partial \mathbf{C}}{\partial t} + \mathbf{v}\cdot\nabla\mathbf{C} - (\nabla\mathbf{v})^T\cdot\mathbf{C} - \mathbf{C}\cdot\nabla\mathbf{v}$.

Scaling lengths, velocities, and time by $R$, $V_z$, and $V_z/R$, respectively, make the governing equations dimensionless. This yields three dimensionless parameters: (1) the Deborah number $De = \lambda V_z/R$ characterizing the polymer relaxation time $\lambda$ to the rate of deformation; (2) the ratio of the solvent viscosity $\eta_s$ to the total viscosity, $\beta = \eta_s/(\eta_s + \eta_{p,\infty})$, where $\eta_{p,\infty} = n_\infty\lambda k_BT$ is the far-field polymeric viscosity; and (3) the ratio of the rotational tangential velocity (from colloidal rotation) to the translational velocity, $\Omega^* = \Omega R/V_z$. Dimensionless variables are marked with asterisks hereafter.

Since the experiments showed a quadratic relationship $V_x \propto -\Omega V_z$[5], we expect a perturbation expansion of Equations 1 and 2, valid for $De \ll 1$, to yield a similar scaling. To order zero in $De$, the flow and stress fields are linearly proportional to the velocity, and the Magnus effect is forbidden. To first order in $De$, these fields are quadratic in the velocity, and we may expect a nonzero migration velocity $V_x$. By performing the expansion up to this order, we obtain $V_x^* = De\, V_{x,1}^* + \mathcal{O}(De^2)$ and then determine the first-order correction $V_{x,1}^*$ using the Lorentz reciprocal theorem[11,41] (see methods). Surprisingly, we find $V_{x,1}^* = 0$, consistent with three-dimensional (3D) numerical solutions to Equations 1 and 2 obtained by a finite element method (FEM), indicating no transversal migration (see methods). We conclude that the OB model—encompassing viscoelastic memory and the first normal-stress difference—fails to account for the Magnus effect observed experimentally. One possible reason for the OB model's failure is its inability to capture shear thinning or the second normal-stress difference. However, by employing the Giesekus model, which extends the OB model by incorporating a second normal-stress difference and shear-thinning properties,[38] we also obtain no lateral colloidal migration (see methods).

## Rethinking the assumption of uniform polymer distribution

This discrepancy with the experiments prompts a reevaluation of whether the assumptions inherent in the OB model align with the experimental conditions. Specifically, we reconsider the assumption of a homogeneous distribution of macromolecules adopted in the OB model. Indeed, the original OB model assumes that the transport of macromolecules with a diffusion coefficient of $D$ is dominated by advection, the Péclet number $Pe = V_zR/D \to \infty$. As a consequence, the model neglects any relative motion between the polymers and the fluid flow, which preserves a homogeneous distribution.

However, this might not be true for flows past micron-sized objects such as those used in the experiments. At such small scales, polymers can be sufficiently extended to sense the curvature of the streamlines around the colloid, and the resulting gradients of stress drive the transport of polymers[42–47] from high-strain to low-strain regions. The physical picture is that macromolecules in inhomogeneous flows tend to migrate away from high-strain-rate regions, thereby avoiding substantial stretching. If the rate of stress-gradient-induced transport is faster or comparable to advection, then the polymers will be distributed inhomogeneously. The relative importance of advection to the stress-gradient-induced transport is quantified by the ratio $Pe/De = R^2/\lambda D$.[48] For a given polymer solution, this ratio depends on the particle size only. For $Pe/De \gg 1$, advection dominates, and the OB model is applicable, while for $Pe/De \lessapprox 1$, we expect considerable polymer density inhomogeneities. By using a characteristic value of diffusion coefficient $D \approx 10^{-12}$ m$^2$s$^{-1}$ and the experimental values $R \approx 2$ μm and $\lambda \approx 1$–10 s,[5,49] we estimate $Pe/De \approx 4$–0.4, indeed suggesting that stress-gradient-induced transport of polymers is comparable or even stronger than advection in the experiments.

The importance of polymer concentration inhomogeneities was realized already by Cao et al.,[5] who incorporated it into a phenomenological model. They assume that a translational motion of the colloid drives a polymer concentration dipole, which is related to an external force through a generic memory kernel. They further assume that the colloidal rotation tilts the dipole away from the colloid's translational direction. Finally, by considering an elastic restoring force directed along the dipole, they obtain a velocity perpendicular to both the angular velocity and the translation direction, yielding the Magnus effect. In what follows, we provide a microscopic mechanism for the emergence of the dipolar polymer concentration. We further show that neither a misalignment between this dipole and the colloidal translation nor a viscoelastic memory kernel is required to explain the colloid's Magnus migration.

## Incorporating stress-gradient-induced polymer transport and inhomogeneity

To account for this effect, we model the spatial-temporal evolution of polymer number density, $n$, subject to the stress gradient, $\nabla\cdot\boldsymbol{\tau}$. Following Apostolakis et al.,[40] Mavrantzas and Beris,[47] and Tsouka et al.[48] within a two-fluid (polymer additives and Newtonian solvent) model, we augment the advection-diffusion transport of polymers with the stress-gradient-induced polymer flux $D\nabla\cdot\boldsymbol{\tau}/(k_BT)$, leading to the governing equation for $n$:

$$\frac{\partial n}{\partial t} + \mathbf{v}\cdot\nabla n = D\nabla\cdot\left(\nabla n - \frac{1}{k_BT}\nabla\cdot\boldsymbol{\tau}\right). \qquad \text{(Equation 3)}$$

The transport of polymers due to stress gradients was proposed phenomenologically by Helfand and Fredrickson[44] to explain polymer migration but was also employed to explain the flow-concentration coupling of worm-like micelles.[50,51] Accordingly, the polymer viscosity, $\eta_p = n\lambda k_BT$, changes locally due to the inhomogeneous polymer density, $n$. The far-field polymer density remains as $n = n_\infty$, while polymers cannot penetrate the particle surface, $(\nabla n - \nabla\cdot\boldsymbol{\tau}/k_BT)\cdot\boldsymbol{n} = 0$. We make the number density dimensionless using $n_\infty$, i.e., $n^* = n/n_\infty$, and report the full dimensionless equations in the methods.

Please cite this article in press as: De Corato et al., Colloidal Magnus effect in polymer solutions, Newton (2025), https://doi.org/10.1016/j.newton.2025.100373



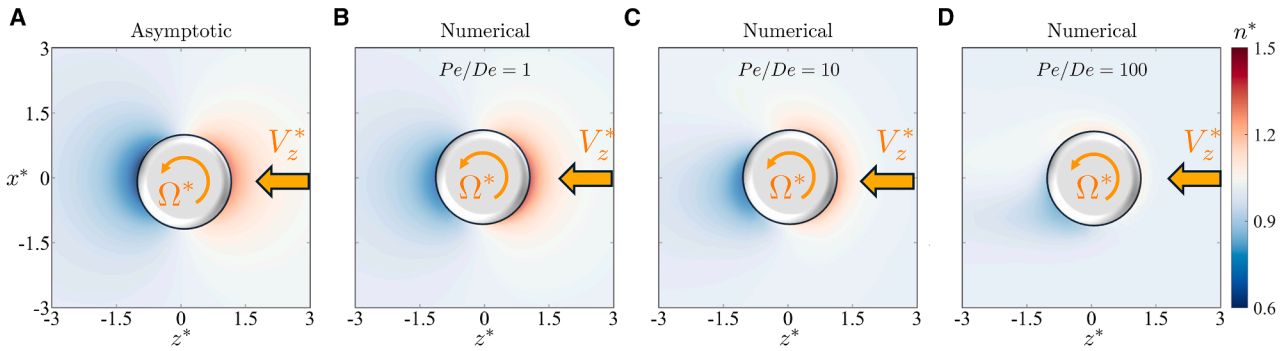


**Figure 2. Distributions of polymer number density $n^*$ in the symmetry plane $y^* = 0$**

(A) Spatial distribution of $n^*$ at $De = 0.3$ as given by the asymptotic formula Equation 4.

(B–D) Numerical predictions of $n^*$ distributions at increasing $Pe/De$ values. When $Pe/De \gg 1$, advection dominates, leading the polymer distribution to approach a homogeneous state. The remaining parameters are $\Omega^* = 0.5$, $De = 0.3$, and $\beta = 0.1$. Here, the orange arrows denote the orientation of flow with respect to the colloid.

We perform a perturbation expansion of Equations 1, 2, and 3, valid for small $De$ and $Pe$ numbers (see methods). To first order in $De$ and $Pe$, we identify an inhomogeneous distribution of number density,

$$n^* = 1 + \frac{3De\, z^*}{2(r^*)^3} + \mathcal{O}(De^2, De\, Pe), \qquad \text{(Equation 4)}$$

where $r^*$ is the dimensionless distance from the origin. Notably, the first-order density deviation, $3De\, z^*/2(r^*)^3$, from the far-field state, $n^*_\infty = 1$, depends solely on $De$ and is independent of the rotational rate, $\Omega$. Linearly proportional to $z^*$, this deviation indicates a dipolar distribution of polymers, revealing their accumulation at the front ($z^* > 0$) and depletion at the rear ($z^* < 0$) of the moving particle (see Figure 2A). While the emergence of a concentration dipole was postulated in Cao et al.[5] based on a phenomenological model, we elucidate here its microscopic origin. The asymptotic solution, Equation 4, agrees with simulations up to $Pe/De \approx 10$ for $De = 0.3$ and $\Omega^* = 0.5$. Remarkably, the perturbation expansion remains valid even when flow advection exceeds stress-gradient-induced transport of polymers. At large $Pe/De$, the concentration dipole tilts away from the colloid's translational orientation ($\mathbf{e}_z$) (see Figures 2C and 2D), a signature of growing rotational convection effect—as also identified by Cao et al.[5]

## Asymptotic predictions capture experimental data without fitting

By further extending the asymptotic analysis through the Lorentz reciprocal theorem, we derive the leading-order transversal velocity of the colloid, signifying the Magnus effect (see methods):

$$V_x^* = -\frac{(1-\beta)De\,\Omega^*}{4}, \qquad \text{(Equation 5)}$$

with its dimensional form:

$$V_x = -\frac{\lambda \eta_{p,\infty} V_z\, \Omega}{4(\eta_s + \eta_{p,\infty})}. \qquad \text{(Equation 6)}$$

This asymptotic prediction captures the experimentally identified trend, $V_x/V_z = -\alpha\,\Omega$ (where $\alpha > 0$),[5] in both sign and scaling, as further examined below. Moreover, Equation 5 is cross-validated against FEM simulations, as evidenced in Figure 3. In the weak rotation limit, $\Omega^* \ll 1$, the numerical and theoretical data match closely for small $De$ (e.g., 0.1) and $Pe/De$ (e.g., 0.1 and 1). However, deviations emerge when $De \gtrsim 0.3$ and systematically grow with $\Omega^*$. Evidently, as the colloid spins faster, the numerical results fall increasingly below the linear asymptotic trend. Specifically at $De = 0.3$, they approach a saturated value when $Pe/De = 0.1$ (see Figure 3A) or 1 (see Figure 3B), similar to the velocity saturation reported in the experiments.[5] It is not surprising that the numerical results shown in Figures 3A–3C deviate from the asymptotic theory as $\Omega^*$ increases. The latter is only valid for $\Omega^* \approx \mathcal{O}(1)$, and it breaks down at $\Omega^* \approx \mathcal{O}(1/De)$ even for small $De$.

Additionally, simulations performed at $\Omega^* = 0.5$ show that the velocity decreases with increasing $Pe/De$, eventually becoming negligible when $Pe/De = 100$ (see Figure 3D). Indeed, in this regime of dominant advection, the OB model is recovered, resulting in no colloid migration, as we find in our initial attempt. In the opposite limit—$Pe = 0$ (no advection) and $Pe/De = 0.1$ (weak advection)—the numerical data for both cases nearly overlap and quantitatively reproduce the asymptotic linear dependence of $-V_x^*$ on $De$ at low values of $De$. Beyond that regime, the velocity changes non-monotonically with $De$ and peaks at $De \approx 1$. Notably, such a peak was reported in studies of micro-locomotion in viscoelastic fluids.[52,53]

We now apply the numerically validated theory to characterize the experimental observations of Cao et al.[5] on colloidal trimers in a micellar solution. Its rheological properties, measured and previously reported by the same group,[49] make this characterization possible. Particularly, these properties include $\lambda \approx 0.9$ s (see methods) and $\eta_{p,\infty}/(\eta_s + \eta_{p,\infty}) \to 1$ (see methods). Using the experimental colloid radius $R \approx 2$ μm and maximum speed $V_z \sim 0.17$ μm s$^{-1}$, we find that $De \approx 0.07 \ll 1$ in the experiments, consistent with the small-$De$ limit assumed in the asymptotic theory. Further, by taking a characteristic diffusion coefficient $D \approx 10^{-12}$ m$^2$s$^{-1}$, the experimental Péclet number is approximately $Pe \approx 0.3$. The errors associated with the asymptotic analysis are of orders $\mathcal{O}(De^2)$ and $\mathcal{O}(De\, Pe)$, which are both small.

Please cite this article in press as: De Corato et al., Colloidal Magnus effect in polymer solutions, Newton (2025), https://doi.org/10.1016/j.newton.2025.100373



CellPress
OPEN ACCESS

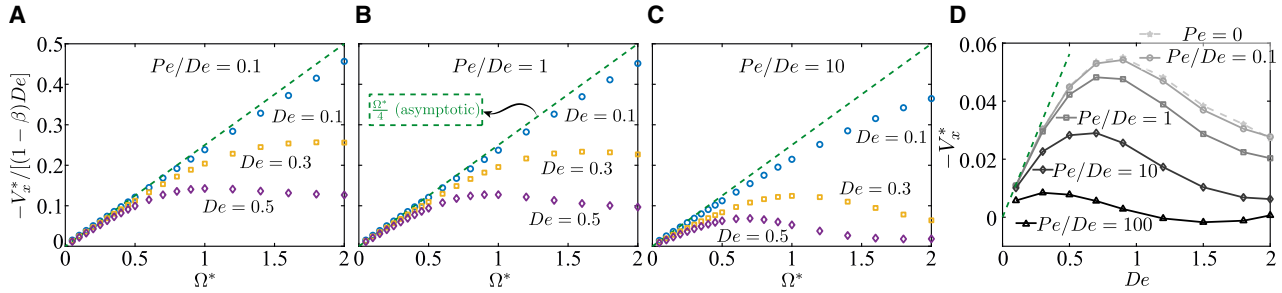


**Figure 3. Numerical Magnus velocity $-V_x^*$ compared to the asymptotic prediction, Equation 5, versus the particle's dimensionless spinning rate $\Omega^*$**

(A–C) The ratio of advection to stress-gradient-induced transport is (A) weak, *Pe*/*De* = 0.1; (B) intermediate, *Pe*/*De* = 1; and (C) strong, *Pe*/*De* = 10. (D) $-V_x^*$ versus *De* at a varying *Pe*/*De* ∈ [0, 100] when $\Omega^*$ = 0.5. Here, $\beta$ = 0.1.

This suggests that the asymptotic theory should be applicable to the experiments of Cao et al.[5]

Indeed, by substituting the experimental values into Equation 6, a quantitative agreement emerges between the theory and experiments (see Figure 4A), where the trimers were forced to translate at three speeds and spin at various rates. A similar agreement holds for a trimer spinning at $|\Omega| \approx 1.2\ \mathrm{s}^{-1}$ but translating at various speeds (see Figure 4B). Remarkably, this agreement does not rely on any fitting parameters. Admittedly, the asymptotic prediction overestimates the Magnus effect of strong spinners (large Ω)—a discrepancy that grows more pronounced at higher translational velocities $V_z$ (subject to the increased $\mathbf{e}_z$-oriented force **F**). In fact, numerical simulations have revealed a similar deviation, where a larger $De = \lambda V_z/R$ in simulations corresponds to a higher $V_z$ in experiments (see Figures 3A–3C). Indeed, as *De* increases, higher-order effects become increasingly important, leading to larger deviations from the asymptotic theory. Note that in the experiment, the authors used a colloidal trimer, while we consider a spherical colloid here. Nevertheless, in the methods, we show that the trimer's lateral migration, which is much harder to compute than that of a sphere, closely agrees with that of a volume-matched sphere.

Based on our findings, we attribute the experimentally observed Magnus effect to two mechanisms. First, the colloidal translation and the concomitant stress-gradient-induced transport cause the polymer concentration, *n*, to be higher at the front and lower at the rear of the colloid, yielding a dipolar distribution of polymeric viscosity, $\eta_p = n\lambda k_B T$, around it. Notably, the quantitative velocity prediction of our asymptotic theory (Equation 6) implies a concentration dipole perfectly aligned with the colloid's forced translational direction, $\mathbf{e}_z$. This contrasts with the misalignment highlighted by Cao et al.[5] as the key mechanism driving their reported colloidal migration. Second, the colloidal rotation in such a viscosity profile results in a fore-aft stress imbalance, driving the transversal migration. Indeed, the migration velocity, Equation 5, is very similar to that of a force-free sphere rotating in a Newtonian fluid with a small viscosity gradient aligned along the *z* axis.[54] This analogy indirectly suggests that the Magnus effect stems purely from the spatial viscosity variation due to an inhomogeneous polymer distribution. Normal-stress differences and shear thinning might play a secondary role, most likely becoming important at much higher *De* numbers. These findings align with recent studies highlighting the importance of local microstructure and viscosity inhomogeneities in the dynamics of active particles.[54–62]

## DISCUSSION

By testing OB fluids, we have established that the inverse Magnus migration of a spherical colloid and a trimer, experimentally observed in polymeric solutions,[5] cannot be explained by normal-stress differences—a typical driver for many other colloidal migration phenomena. Shear-thinning rheology modeled

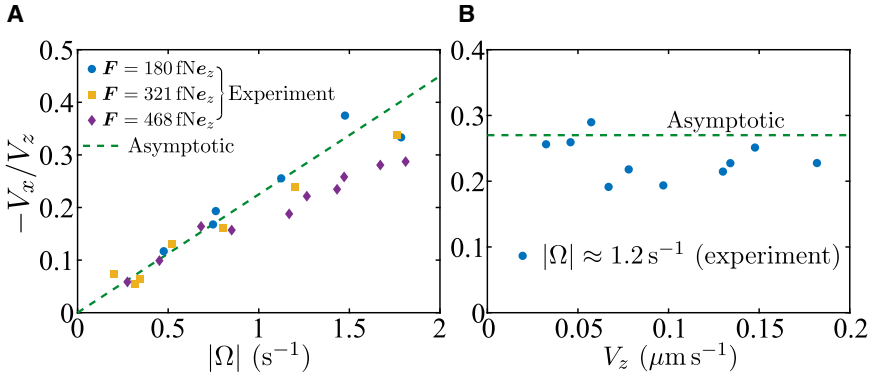


**Figure 4. Quantitative agreement between our asymptotic prediction, Equation 6, and the experimental results for a rotating trimer in a micellar solution**

It experienced (A) three $\mathbf{e}_z$-oriented forces **F** with various rotating speeds |Ω| and (B) varying translational velocities $V_z$ at a prescribed $|\Omega| \approx 1.2\ \mathrm{s}^{-1}$. See Figure 1B. Adapted from Cao et al.[5] under CC BY 4.0 (https://creativecommons.org/licenses/by/4.0/).

Please cite this article in press as: De Corato et al., Colloidal Magnus effect in polymer solutions, Newton (2025), https://doi.org/10.1016/j.newton.2025.100373



by the Giesekus model likewise fails to explain this migration. Instead, our analysis reveals that the effect arises from a dipolar distribution of polymer density and the resulting dipolar profile of local viscosity. As a side note, we find that particle shape (sphere or trimer) plays a minor role.

While a polymer density dipole was phenomenologically proposed in Cao et al.[5] to model migration—attributed to finite polymer stress-relaxation time—the inability of the standard OB model (treating polymers as Hookean dumbbells) to reproduce migration indicates that stress relaxation alone is insufficient for the polar polymer-density distribution or, more broadly, any marked inhomogeneity. Theory,[63] experiments,[64] and simulations[65] imply that polymer relaxation is neither necessary nor sufficient for such inhomogeneous distributions (see discussions in the methods).

Indeed, using cross-validated theoretical modeling and numerical simulations, we have identified the microscopic origin of the dipole: stress-gradient-induced transport of polymers. Stress-gradient-induced migration of microstructure has been largely overlooked in the context of colloidal motion through complex fluids, despite representing a general mechanism applicable beyond the current observation. We speculate that the Magnus effect described here may occur on colloids translating and spinning in other microstructured flows where coupling between the flow and microstructure concentration plays an important role.[66,67] However, additional experiments considering different kinds of microstructured liquids are required to confirm this speculation.

Crucially, our mechanistic interpretation is validated by the quantitative agreement between experimental data and our theoretical model, which incorporates these mechanisms—notably, without adjustable parameters. Finally, our results underscore the necessity of reassessing standard constitutive models predicated on homogeneous polymer distributions, both for modeling the behavior of (sub)micro-scale objects—including passive and self-propelling colloids,[68] microorganisms,[69] and microrobots[70]—in complex fluids and, more broadly, in (sub)micro-scale polymeric flows. In these cases, macromolecules can feel the curvature of the streamlines, leading to significant concentration inhomogeneities, which can play a more important role than viscoelastic stresses. From an application perspective, our results would inform strategies for steering and controlling colloids in microfluidic setups via external fields. However, throughput might be limited by the small lateral migration speeds, typically hundreds of nanometers per second.

## METHODS

### OB and Giesekus models

Using the characteristic scales defined in the main text, we obtain the dimensionless governing equations. The momentum balance and continuity equations are

$$\nabla^*\cdot(2\beta\mathbf{E}^* - p^*\mathbf{I} + \boldsymbol{\tau}^*) = \mathbf{0} \text{ and } \nabla^*\cdot\mathbf{v}^* = 0. \quad \text{(Equation 7)}$$

The OB model for the polymeric stress is

$$De\,\overset{\nabla}{\boldsymbol{\tau}}^* + \boldsymbol{\tau}^* = 2(1-\beta)\,\mathbf{E}^*, \quad \text{(Equation 8)}$$

and the Giesekus counterpart is

$$De\,\overset{\nabla}{\boldsymbol{\tau}}^* + \boldsymbol{\tau}^* + \frac{\alpha\,De}{1-\beta}\boldsymbol{\tau}^*\cdot\boldsymbol{\tau}^* = 2(1-\beta)\mathbf{E}^*, \quad \text{(Equation 9)}$$

where $\alpha$ must be between 0 and 1.[38] The force-free condition is given by

$$\int_S (2\beta\mathbf{E}^* - p^*\mathbf{I} + \boldsymbol{\tau}^*) : \mathbf{n}\mathbf{e}_x dS = 0. \quad \text{(Equation 10)}$$

The velocity far from the particle is

$$\mathbf{v}^* = -\mathbf{e}_z - V_x^*\mathbf{e}_x, \quad \text{(Equation 11)}$$

and that at the particle surface reads

$$\mathbf{v}^* = \Omega^*\mathbf{e}_y \times \mathbf{r}^*. \quad \text{(Equation 12)}$$

Perturbation expansion: we seek a solution in the form of a perturbation expansion for small $De$ values, expanding the relevant variables as $\mathbf{v}^* = \mathbf{v}_0^* + De\,\mathbf{v}_1^* + \mathcal{O}(De^2)$, $p^* = p_0^* + De\,p_1^* + \mathcal{O}(De^2)$, $\boldsymbol{\tau}^* = \boldsymbol{\tau}_0^* + De\,\boldsymbol{\tau}_1^* + \mathcal{O}(De^2)$, and $V_x^* = De\,V_{x,1}^* + \mathcal{O}(De^2)$.

Zeroth-order problem: the zero-order equations are obtained by substituting the perturbation expansion into the main equations and retaining only the terms that do not depend on $De$. The polymeric stress is $\boldsymbol{\tau}_0^* = 2(1-\beta)\mathbf{E}_0^*$. The zeroth-order momentum and continuity equations are

$$\nabla^*\cdot(2\mathbf{E}_0^* - p_0^*\mathbf{I}) = \mathbf{0} \text{ and } \nabla^*\cdot\mathbf{v}_0^* = 0, \quad \text{(Equation 13)}$$

corresponding to the Newtonian Stokes flow. Its flow field can be obtained by superimposing the flow past a sphere and that around a spinning sphere, resulting in

$$\mathbf{v}_0^* = \mathbf{e}_z\cdot\left[\left(\frac{3}{4r^*} + \frac{1}{4r^{*3}}\right)\mathbf{I} + \frac{3}{4}\left(\frac{1}{r^{*3}} - \frac{1}{r^{*5}}\right)\mathbf{r}^*\mathbf{r}^*\right] + \Omega^*\mathbf{e}_y\times\mathbf{r}^*\Big/r^{*3} - \mathbf{e}_z. \quad \text{(Equation 14)}$$

First-order problem: the first-order equations are obtained by substituting the perturbation expansion into the equations and retaining only the terms proportional to $De$. The first-order solution of the polymeric stress is

$$\boldsymbol{\tau}_1 = 2(1-\beta)\mathbf{E}_1^* - \overset{\nabla}{\boldsymbol{\tau}}_0^* \quad \text{(Equation 15)}$$

for the OB fluid and

$$\boldsymbol{\tau}_1 = 2(1-\beta)\mathbf{E}_1^* - \overset{\nabla}{\boldsymbol{\tau}}_0^* - \frac{\alpha\,De}{1-\beta}\boldsymbol{\tau}_0^*\cdot\boldsymbol{\tau}_0^* \quad \text{(Equation 16)}$$

for the Giesekus model. In the equations above, $\overset{\nabla}{\boldsymbol{\tau}}_0^*$ is a shorthand notation for

$$\overset{\nabla}{\boldsymbol{\tau}}_0^* = \mathbf{v}_0^*\cdot\nabla\boldsymbol{\tau}_0^* - \left(\nabla\mathbf{v}_0^*\right)^T\cdot\boldsymbol{\tau}_0^* - \boldsymbol{\tau}_0^*\cdot\nabla\mathbf{v}_0^*. \quad \text{(Equation 17)}$$

The momentum and continuity equations are

$$\nabla\cdot(2\beta\mathbf{E}_1^* - p_1^*\mathbf{I} + \boldsymbol{\tau}_1^*) = \mathbf{0} \text{ and } \nabla\cdot\mathbf{v}_1^* = 0. \quad \text{(Equation 18)}$$

Please cite this article in press as: De Corato et al., Colloidal Magnus effect in polymer solutions, Newton (2025), https://doi.org/10.1016/j.newton.2025.100373



CellPress
OPEN ACCESS

The far-field velocity $\mathbf{v}_1^* = -V_{x,1}^*\mathbf{e}_x$, and $\mathbf{v}_1^* = \mathbf{0}$ at the particle surface. The first-order force-free condition is $\int_S(2\beta\mathbf{E}_1^* - p_1^*\mathbf{I} + \boldsymbol{\tau}_1^*):\mathbf{n}\mathbf{e}_x dS = 0$.

Generalized reciprocal theorem: using the Lorentz reciprocal theorem,[11,41,71] we compute the first-order velocity $V_{x,1}^*$ by the volume integral over the fluid domain, $\mathcal{V}$. For the OB model,

$$V_{x,1}^* = \frac{1}{6\pi}\int_{\mathcal{V}}\nabla\widehat{\mathbf{v}}^* : \overset{\nabla}{\boldsymbol{\tau}}_0^* d\mathcal{V}, \qquad \text{(Equation 19)}$$

where $\widehat{\mathbf{v}}^*$ is an auxiliary velocity field corresponding to Newtonian Stokes flow with an ambient velocity $1\mathbf{e}_x$ past a stationary sphere, that is,

$$\widehat{\mathbf{v}}^* = \mathbf{e}_x - \mathbf{e}_x\cdot\left[\left(\frac{3}{4r^*} + \frac{1}{4r^{*3}}\right)\mathbf{I} + \frac{3}{4}\left(\frac{1}{r^{*3}} - \frac{1}{r^{*5}}\right)\mathbf{r}^*\mathbf{r}^*\right]. \qquad \text{(Equation 20)}$$

The integration in Equation 19 involves multiplication of quantities known analytically from the zeroth-order problem and can therefore be evaluated symbolically, as we do in Wolfram Mathematica. Specifically, we employ spherical coordinates and first perform the angular integrations to obtain

$$V_{x,1}^* = -\frac{(\beta-1)\Omega^*}{6\pi}\int_{r^*=1}^{\infty}\frac{[3(r^*-1)r^* - 5]\,r^{*3}+6}{r^{*9}}dr^*. \qquad \text{(Equation 21)}$$

It is straightforward to show that the resulting integral is zero. Likewise, for the Giesekus model,

$$V_{x,1}^* = \frac{1}{6\pi}\int_{\mathcal{V}}\nabla\widehat{\mathbf{v}}^* : \left(\overset{\nabla}{\boldsymbol{\tau}}_0^* - \frac{\alpha\,De}{1-\beta}\boldsymbol{\tau}_0^*\cdot\boldsymbol{\tau}_0^*\right)d\mathcal{V}. \qquad \text{(Equation 22)}$$

We have already shown that the integral of the first term in the bracket is zero. Using Wolfram Mathematica, we find that the integral of the second term is also zero.

## Stress-gradient-induced polymer transport

The OB and Giesekus models assume a uniform far-field number density $n = n_\infty$. Here, we extend the OB model by incorporating a non-uniform density $n$. Taking $n_\infty$ as the characteristic scale, the dimensionless number density $n^* = n/n_\infty$. While the momentum and continuity equations remain unchanged, the polymeric stress follows an adapted constitutive law[40,48]

$$De\overset{\nabla}{\boldsymbol{\tau}}^* + \boldsymbol{\tau}^* + (1-\beta)\left(\frac{Dn^*}{Dt^*}\right)\mathbf{I} = 2(1-\beta)n^*\mathbf{E}^*, \qquad \text{(Equation 23)}$$

where $D()/Dt^*$ denotes the material derivative. Specifically, the spatiotemporal evolution of $n^*$ is governed by

$$Pe\frac{Dn^*}{Dt^*} = \nabla\cdot\left(\nabla n^* - \frac{De}{1-\beta}\nabla\cdot\boldsymbol{\tau}^*\right). \qquad \text{(Equation 24)}$$

The force-free condition and boundary conditions for the velocity are the same as Equations 10, 11, and 12. The boundary condition for $n^*$ at the particle surface reads

$$\mathbf{n}\cdot\left(-\nabla n^* + \frac{De}{1-\beta}\nabla\cdot\boldsymbol{\tau}^*\right) = 0, \qquad \text{(Equation 25)}$$

and that far from the particle is $n^* = 1$.

Perturbation expansion: we seek a solution in the form of a perturbation expansion for small $De$ and $Pe$. We find that all asymptotic terms proportional to powers of $Pe$ only are zero. The variables are expanded as $\mathbf{v}^* = \mathbf{v}_0^* + De\,\mathbf{v}_1^* + \mathcal{O}(De^2, De\,Pe)$, $p^* = p_0^* + De\,p_1^* + \mathcal{O}(De^2, De\,Pe)$, $\boldsymbol{\tau}^* = \boldsymbol{\tau}_0^* + De\,\boldsymbol{\tau}_1^* + \mathcal{O}(De^2, De\,Pe)$, $n^* = 1 + De\,n_1^* + \mathcal{O}(De^2, De\,Pe)$, and $V_x^* = De\,V_{x,1}^* + \mathcal{O}(De^2, De\,Pe)$.

Zeroth-order problem: the zeroth-order equations and their solutions, $\mathbf{v}_0^*$ and $p_0$, are the same as those for the OB and Giesekus models because the zeroth-order polymer density is uniformly equal to its far-field value.

First-order problem: the first-order polymeric stress takes the form

$$\boldsymbol{\tau}_1^* = 2(1-\beta)(n_1^*\mathbf{E}_0^* + \mathbf{E}_1^*) - \overset{\nabla}{\boldsymbol{\tau}}_0^* - (1-\beta)\left(\frac{Dn_1^*}{Dt}\right)\mathbf{I}. \qquad \text{(Equation 26)}$$

We note that the last term is an isotropic tensor not contributing to the velocity field. It can be absorbed by defining a modified $P_1^* = p_1^* + (1-\beta)Dn_1^*/Dt$, yielding

$$\boldsymbol{\tau}_1^* = 2(1-\beta)(n_1^*\mathbf{E}_0^* + \mathbf{E}_1^*) - \overset{\nabla}{\boldsymbol{\tau}}_0^*. \qquad \text{(Equation 27)}$$

The momentum and continuity equations are $\nabla\cdot(2\beta\mathbf{E}_1^* - P_1^*\mathbf{I} + \boldsymbol{\tau}_1^*) = \mathbf{0}$ and $\nabla\cdot\mathbf{v}_1^* = 0$. The velocity far from the particle is $\mathbf{v}_1^* = -V_{x,1}^*\mathbf{e}_x$, and at the particle surface, $\mathbf{v}_1^* = \mathbf{0}$. The force-free condition is $\int_{S^*}(2\beta\mathbf{E}_1^* - P_1^*\mathbf{I} + \boldsymbol{\tau}_1^*):\mathbf{n}\mathbf{e}_x dS^* = 0$. To proceed, we first solve for the number density $n_1^*$. Its steady-state solution follows

$$\nabla\cdot\left(\nabla n_1^* - \frac{1}{1-\beta}\nabla\cdot\boldsymbol{\tau}_0^*\right) = 0, \qquad \text{(Equation 28)}$$

which can be reduced to the Laplace equation $\nabla^2 n_1^* = 0$, realizing $\nabla\nabla:\boldsymbol{\tau}_0^* = 0$. The zero-flux boundary condition at the particle surface becomes

$$\mathbf{n}\cdot\left(-\nabla n_1^* + \frac{1}{1-\beta}\nabla\cdot\boldsymbol{\tau}_0^*\right) = 0, \qquad \text{(Equation 29)}$$

and $n_1^* = 0$ in the far field. We obtain $n_1^* = 3z^*/2r^{*3}$ that is independent of $\Omega^*$, implying that the particle rotation does not cause the polymer inhomogeneity at the first order.

Generalized reciprocal theorem: employing again the reciprocal theorem, we derive the first-order velocity as

$$V_{x,1}^* = \frac{1}{6\pi}\int_{\mathcal{V}}\nabla\widehat{\mathbf{v}}^* : [2(1-\beta)n_1^*\mathbf{E}_0^* + \overset{\nabla}{\boldsymbol{\tau}}_0^*]\,d\mathcal{V}, \qquad \text{(Equation 30)}$$

where $\widehat{\mathbf{v}}^*$ is the auxiliary flow field introduced in Equation 20. Noting that the integral involving $\overset{\nabla}{\boldsymbol{\tau}}_0^*$ is identical to that for the

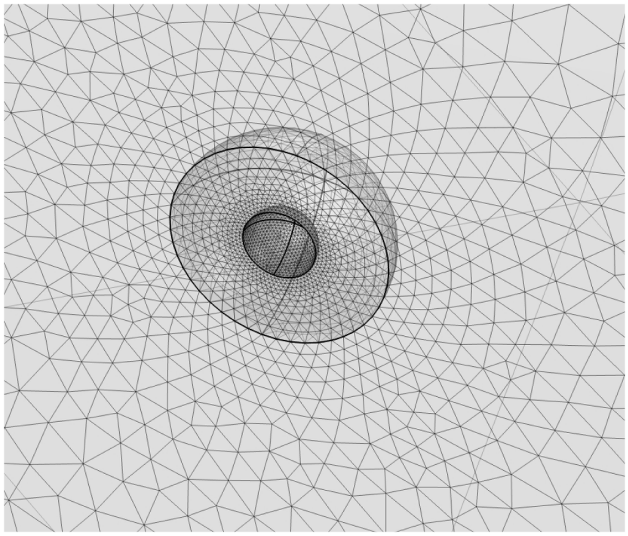

**Figure 5. An illustration of near-particle elements with a minimum element size of 0.1**

OB model (see Equation 19) and is thus zero, the first-order velocity is given by

$$V^*_{x,1} = \frac{1}{6\pi}\int_{\mathcal{V}} \nabla\hat{\mathbf{v}}^* : \left[2(1-\beta)n^*_1\mathbf{E}^*_0\right]d\mathcal{V}, \qquad \text{(Equation 31)}$$

which crucially depends on the first-order inhomogeneous polymer distribution $n^*_1$ derived above. The integral is evaluated analytically using Wolfram Mathematica.

## Numerical methods

We solve the dimensionless equations using the FEM package, COMSOL Multiphysics, employing its partial differential equation interface. Specifically, we solve Equation 7 for fluid motion, combined with Equation 8 for the OB model or Equation 9 for the Giesekus counterpart, or Equations 23 and 24 when considering stress-gradient-induced polymer transport.

Exploiting the mirror symmetry about the $x^*z^*$ plane, we consider a fluid domain in the form of a semi-spherical shell with an inner radius of 1 and an outer radius of 200. The inner and outer boundaries represent the particle surface and far field, respectively.

The domain is discretized by ≈ 198,000 tetrahedral elements, with polynomial order two for velocity $\mathbf{u}^*$ and order one for the other variables (pressure $p^*$, polymeric stress $\boldsymbol{\tau}^*$, and number density $n^*$), respectively. The mesh is refined near the particle surface, yielding a minimum element size of 0.1 (see Figure 5). We perform a mesh-independence study, as summarized in Table 1. An investigation into the domain size, summarized in Table 2, indicates that the selected domain is sufficiently large.

To stabilize the simulations, streamline diffusion is applied to the equations for $\boldsymbol{\tau}^*$ and $n^*$. Imposing the force-free condition to compute the migration velocity of particles is achieved through a "Global Equations" node. We solve the steady-state equations (removing the time-derivative terms) in a fully coupled manner, utilizing the direct solver MUMPS with a relative tolerance of $1 \times 10^{-8}$.

## Magnus effect for a colloidal trimer

Besides the spherical colloid presented in the main text, we have also numerically investigated the Magnus migration of a volume-matched colloidal trimer. Notably, trimers were mostly examined in the experiments[5] for their visualization advantages over spheres—yet simulating a trimer is substantially more challenging, as detailed below.

We build the trimer by unifying three spheres of radius $R_t$ centered at the vertices of an equilateral triangle, as shown in Figure 6A. Each sphere center is offset from the trimer center by the radius, i.e., $R_t$. We choose $R_t$ so that the trimer volume matches that of the spherical colloid of radius $R$. As for the sphere, we harness the mirror symmetry about the $y$ = 0 plane and compute on half of the domain. The 3D geometry and corresponding mesh are shown in Figure 6B.

Like the spherical colloid, the trimer is forced to translate at a constant velocity $V_z\mathbf{e}_z$ and to rotate constantly at $\Omega$ about the $y$ axis, hence potentially migrating laterally along the $x$ axis with velocity $V_x$. While the governing equations, boundary conditions, and colloidal force balance remain the same, it is considerably more complicated to simulate a trimer. The complication arises from its 3-fold rotational symmetry: the trimer's orientation relative to the imposed translation along $\mathbf{e}_z$ varies periodically in time. Consequently, the flow and colloidal kinematics are unsteady—unlike the steady scenario of a sphere—so time-dependent simulations are required. We employ an arbitrary Lagrangian-Eulerian (ALE) approach[72] in COMSOL by rotating the entire mesh with the trimer's angular velocity. This avoids mesh distortion and the otherwise inevitable, cumbersome remeshing.

As expected, the lateral migration velocity of the trimer oscillates periodically in time. Its dimensionless velocity $V^*_x$ over one period is plotted in Figure 6C, alongside the sphere's time-independent values, where $De$ = 0.3, $Pe$ = 0.03, and $\beta$ = 0.1. Notably, these oscillations are typically within 10% of the period-averaged velocity. More importantly, despite the geometric difference, this average of the trimer agrees reasonably

**Table 1. Mesh dependence evaluated for two cases: #1, $\beta$ = 0.1, $De$ = $Pe$ = 0.3, and $\Omega^*$ = 0.5 and #2, $\beta$ = 0.1, $De$ = 0.5, $Pe$ = 5, and $\Omega^*$ = 1.0**

| Minimum element size | Total number of elements | Migration velocity – $V^*_x$ (case #1) | Migration velocity – $V^*_x$ (case #2) |
|---|---|---|---|
| 0.2 | ≈136,000 | 0.0252 | 0.0190 |
| 0.135 | ≈165,000 | 0.0287 | 0.0217 |
| 0.1 (used in this study) | ≈198,000 | 0.0296 | 0.0237 |
| 0.07 | ≈262,000 | 0.0298 | 0.0227 |
| 0.05 | ≈359,000 | 0.0297 | 0.0222 |

Please cite this article in press as: De Corato et al., Colloidal Magnus effect in polymer solutions, Newton (2025), https://doi.org/10.1016/j.newton.2025.100373



CellPress
OPEN ACCESS

**Table 2. Influence of the domain size—the radius of the outer sphere—on the numerically calculated migration velocity $-V_x^*$ at varying *De* and *Pe* values, where $\Omega^* = 1.0$ and $\beta = 0.1$**

| *De* | *Pe* | $-V_x^*$ (outer radius: 200) | $-V_x^*$ (outer radius: 400) |
|---|---|---|---|
| 0.1 | 1 | 0.019324 | 0.019042 |
| 0.3 | 3 | 0.033575 | 0.033175 |
| 0.5 | 5 | 0.023732 | 0.023342 |
| 0.1 | 0.1 | 0.021349 | 0.021057 |
| 0.3 | 0.3 | 0.052833 | 0.052408 |
| 0.5 | 0.5 | 0.057282 | 0.056870 |
| 0.1 | 0.01 | 0.021456 | 0.021163 |
| 0.3 | 0.03 | 0.055109 | 0.054674 |
| 0.5 | 0.05 | 0.064177 | 0.063743 |

well with the steady velocity of a sphere. This finding supports comparing the experimental data on trimers[5] and our asymptotic predictions for spheres in the main text.

## Rheological properties of the micellar solution

For the theory-experiment comparison shown in Figure 4, the rheological fluid tested by Cao et al.[5] was a wormlike micellar solution composed of about 5 mM equimolar cetylpyridinium chloride monohydrate (CPyCl) and sodium salicylate (NaSal) dissolved in water. Its rheological properties were measured by the same group.[49] As reported, its zero-shear viscosity is 0.045 ± 0.005 Pa·s, substantially larger than the viscosity of water, thereby leading to $\beta \to 0$. The inset of Figure 6C in Gomez-Solano and Bechinger[49] indicates that the solution's largest relaxation time is approximately 0.9 s, which we choose as the relaxation time $\lambda$ in our constitutive model.

## Stress-relaxation of polymers and their dipolar distribution

In the discussion, we have asserted that stress relaxation of polymers alone is neither necessary nor sufficient for their dipolar distribution around the colloid. This argument is supported by prior theoretical,[63] experimental,[64] and numerical[65] studies.

## Theoretical perspective

Even in a Newtonian fluid ($\lambda \to 0$), the theoretical study[63] demonstrates that actively pulling a particle through a colloid suspension results in a fore-aft asymmetric distribution of colloidal density—a "bow wave" of colloids in front and a wake of lowered concentration behind the particle. Notably, the theoretical system exhibiting this asymmetry excludes relaxation, i.e., $\lambda = 0$, indicating that relaxation of suspended microstructures (colloids or polymers) is not a necessary condition for their asymmetric distribution. In fact, this asymmetry is induced by convection and finite colloidal mobility.

## Experimental observations

Experiments on microbeads pulled through polymer solutions (entangled and unentangled)[64] provide direct evidence that stress relaxation ($\lambda$) alone is neither sufficient nor immediately responsible for polymer concentration changes. The experiments observed localized regions of altered polymer density along the

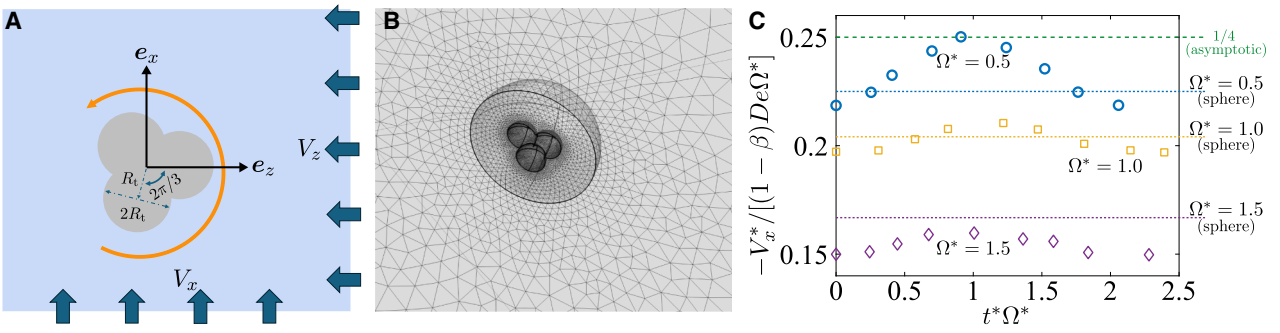


**Figure 6. Numerical simulations of a translating and rotating trimer in viscoelastic fluids**

(A) The trimer is formed by fusing three identical colloids of radius $R_t$, which are centered at the vertices of an equilateral triangle. The colloidal center is offset from the trimer center by $R_t$. $R_t$ is chosen such that the volume of the trimer matches that of the original colloid of radius $R$. The trimer translates along the $z$ axis at a constant velocity, $V_z$, and rotates around the $y$ axis at a constant angular rate, $\Omega$. Its velocity in the $x$ direction, $V_x$, is unknown. The Cartesian reference frame translates with the trimer center.

(B) 3D geometry and corresponding mesh for the simulation of a trimer.

(C) Rescaled migration velocities of a trimer (symbols) over one period for $\Omega^* = 0.5$ (circles), 1.0 (squares), and 1.5 (diamonds). Horizontal lines denote the asymptotic (dashed) and numerically obtained (dotted) steady velocities of a volume-matched sphere. Here, $\beta = 0.1$, $De = 0.3$, and $Pe = 0.03$.

path of a dragged bead. Importantly, once the bead stopped, the polymer density homogenized to equilibrium separately from the stress relaxation of the polymers. Even more, the post-strain homogenization of polymers did not interfere with their intrinsic stress relaxation but rather behaved as an independent mode of stress decay. This implies that a finite relaxation time allowing stored elastic stresses does not by itself suffice to restore uniform polymer density; the polymers must physically move to refill the depleted wake or to dissipate the crowded front.

### Numerical evidence

Zöttl and Yeomans[65] numerically simulate the motion of a particle in explicitly modeled polymer solutions, identifying polymer-rich and polymer-poor regions at the front and rear of the particle when polymers are very dilute (see the first column of Figure 6 in Zöttl and Yeomans[65]). This asymmetric profile originates from convective deformation, namely, the particle forces the polymers out of its way. It pushes polymers forward, causing their accumulation. Conversely, the rear polymer-poor region appears because polymers require time to diffusively re-enter this area. Importantly, this convection-induced inhomogeneity of polymers is unrelated to the their relaxation time. The irrelevance of polymer relaxation is directly supported by the sister work of the same authors,[56] which studies a self-propelled model bacterium in similar polymer solutions. They observe microstructural inhomogeneity even near a bacterium swimming in monomer suspensions (see Figure 3K, right column, in Zöttl and Yeomans[65]), confirming that polymer relaxation time is not necessary for such inhomogeneity.

## RESOURCE AVAILABILITY

### Lead contact

Requests for further information and resources should be directed to and will be fulfilled by the lead contact, Lailai Zhu (lailai_zhu@nus.edu.sg).

### Materials availability

This study did not generate new materials.

### Data and code availability

The COMSOL implementation used in this work is available from the lead contact upon request.

## ACKNOWLEDGMENTS

M.D.C. was supported by Ramon y Cajal fellowship RYC2021-030948-I and by the PID2022-139803NB-I00 research grant funded by the MICIU/AEI/10.13039/501100011033 and by the EU under the NextGenerationEU/PRTR program. L.Z. acknowledges the support from the Singapore Ministry of Education Academic Research Fund Tier 2 grant (MOE-T2EP50221-0012 and MOE-T2EP50122-0015). Some computation of the work was performed on the resources of the National Supercomputing Center, Singapore (https://www.nscc.sg). We thank Xin Cao for initial discussions and Hua Zhang for performing some preliminary simulations. M.D.C. and L.Z. thank Eric Keaveny, Blaise Delmotte, and the European Mechanics Society for the invitation to the 645 EUROMECH Colloquium on Nonlinear Dynamics at Zero Reynolds Numbers, which fostered this collaboration.

## AUTHOR CONTRIBUTIONS

Conceptualization, M.D.C.; methodology, M.D.C. and L.Z.; investigation, M.D.C., K.Z., and L.Z.; writing—original draft, M.D.C. and L.Z.; writing—review & editing, M.D.C. and L.Z.; funding acquisition, M.D.C. and L.Z.; resources, M.D.C. and L.Z.; supervision, M.D.C. and L.Z.

## DECLARATION OF INTERESTS

The authors declare no competing interests.

## DECLARATION OF GENERATIVE AI AND AI-ASSISTED TECHNOLOGIES IN THE WRITING PROCESS

During the preparation of this work, the authors used ChatGPT in order to improve the clarity of the writing. After using this tool or service, the authors reviewed and edited the content as needed and take full responsibility for the content of the publication.

Received: August 4, 2025
Revised: October 16, 2025
Accepted: December 17, 2025

## REFERENCES

1. Chapman, C.D., and Robertson-Anderson, R.M. (2014). Nonlinear microrheology reveals entanglement-driven molecular-level viscoelasticity of concentrated DNA. Phys. Rev. Lett. *113*, 098303.
2. Weissenberg, K. (1947). A continuum theory of rheological phenomena. Nature *159*, 310–311.
3. Giesekus, H. (1965). Some secondary flow phenomena in general viscoelastic fluids. In Proceedings of the Fourth International Congress on Rheology, Part 1.
4. Hill, C.T. (1972). Nearly viscometric flow of viscoelastic fluids in the disk and cylinder system. II: Experimental. Trans. Soc. Rheol. *16*, 213–245.
5. Cao, X., Das, D., Windbacher, N., Ginot, F., Krüger, M., and Bechinger, C. (2023). Memory-induced Magnus effect. Nat. Phys. *19*, 1904–1909.
6. Newton, I. (1993). A new theory about light and colors. Am. J. Phys. *61*, 108–112.
7. Magnus, G. (1853). Ueber die Abweichung der Geschosse, und: Ueber eine auffallende Erscheinung bei rotirenden körpern. Ann. Phys. *164*, 1–29.
8. Karnis, A., and Mason, S.G. (1966). Particle motions in sheared suspensions. XIX. Viscoelastic media. Trans. Soc. Rheol. *10*, 571–592.
9. Ho, B.P., and Leal, L.G. (1976). Migration of rigid spheres in a two-dimensional unidirectional shear flow of a second-order fluid. J. Fluid Mech. *76*, 783–799.
10. Chan, P.C.H., and Leal, L.G. (1977). A note on the motion of a spherical particle in a general quadratic flow of a second-order fluid. J. Fluid Mech. *82*, 549–559.
11. Leal, L.G. (1979). The motion of small particles in non-Newtonian fluids. J. Nonnewton. Fluid Mech. *5*, 33–78.
12. Brunn, P. (1980). The motion of rigid particles in viscoelastic fluids. J. Nonnewton. Fluid Mech. *7*, 271–288.
13. Leshansky, A.M., Bransky, A., Korin, N., and Dinnar, U. (2007). Tunable nonlinear viscoelastic "focusing" in a microfluidic device. Phys. Rev. Lett. *98*, 234501.
14. D'Avino, G., Greco, F., and Maffettone, P.L. (2017). Particle migration due to viscoelasticity of the suspending liquid and its relevance in microfluidic devices. Annu. Rev. Fluid Mech. *49*, 341–360.
15. Yuan, D., Zhao, Q., Yan, S., Tang, S.Y., Alici, G., Zhang, J., and Li, W. (2018). Recent progress of particle migration in viscoelastic fluids. Lab Chip *18*, 551–567.
16. Brunn, P. (1976). The slow motion of a sphere in a second-order fluid. Rheol. Acta *15*, 163–171.

Please cite this article in press as: De Corato et al., Colloidal Magnus effect in polymer solutions, Newton (2025), https://doi.org/10.1016/j.newton.2025.100373



17. Michele, J., Pätzold, R., and Donis, R. (1977). Alignment and aggregation effects in suspensions of spheres in non-Newtonian media. Rheol. Acta *16*, 317–321.

18. D'Avino, G., Snijkers, F., Pasquino, R., Hulsen, M.A., Greco, F., Maffettone, P.L., and Vermant, J. (2012). Migration of a sphere suspended in viscoelastic liquids in Couette flow: experiments and simulations. Rheol. Acta *51*, 215–234.

19. Kim, J.Y., Ahn, S.W., Lee, S.S., and Kim, J.M. (2012). Lateral migration and focusing of colloidal particles and DNA molecules under viscoelastic flow. Lab Chip *12*, 2807–2814.

20. Van Loon, S., Fransaer, J., Clasen, C., and Vermant, J. (2014). String formation in sheared suspensions in rheologically complex media: The essential role of shear thinning. J. Rheol. *58*, 237–254.

21. Lim, H., Nam, J., and Shin, S. (2014). Lateral migration of particles suspended in viscoelastic fluids in a microchannel flow. Microfluid. Nanofluid. *17*, 683–692.

22. Lim, E.J., Ober, T.J., Edd, J.F., Desai, S.P., Neal, D., Bong, K.W., Doyle, P.S., McKinley, G.H., and Toner, M. (2014). Inertio-elastic focusing of bioparticles in microchannels at high throughput. Nat. Commun. *5*, 4120.

23. Seo, K.W., Byeon, H.J., Huh, H.K., and Lee, S.J. (2014). Particle migration and single-line particle focusing in microscale pipe flow of viscoelastic fluids. RSC Adv. *4*, 3512–3520.

24. Li, G., McKinley, G.H., and Ardekani, A.M. (2015). Dynamics of particle migration in channel flow of viscoelastic fluids. J. Fluid Mech. *785*, 486–505.

25. Lu, X., Liu, C., Hu, G., and Xuan, X. (2017). Particle manipulations in non-Newtonian microfluidics: A review. J. Colloid Interface Sci. *500*, 182–201.

26. Jaensson, N.O., Mitrias, C., Hulsen, M.A., and Anderson, P.D. (2018). Shear-induced migration of rigid particles near an interface between a Newtonian and a viscoelastic fluid. Langmuir *34*, 1795–1806.

27. Yu, Z., Wang, P., Lin, J., and Hu, H.H. (2019). Equilibrium positions of the elasto-inertial particle migration in rectangular channel flow of Oldroyd-B viscoelastic fluids. J. Fluid Mech. *868*, 316–340.

28. Zhou, J., and Papautsky, I. (2020). Viscoelastic microfluidics: Progress and challenges. Microsyst. Nanoeng. *6*, 113.

29. Del Giudice, F., Haward, S.J., and Shen, A.Q. (2017). Relaxation time of dilute polymer solutions: A microfluidic approach. J. Rheol. *61*, 327–337.

30. Vishnampet, R., and Saintillan, D. (2012). Concentration instability of sedimenting spheres in a second-order fluid. Phys. Fluids *24*, 073302.

31. Einarsson, J., and Mehlig, B. (2017). Spherical particle sedimenting in weakly viscoelastic shear flow. Phys. Rev. Fluids *2*, 063301.

32. Zhang, A., Murch, W.L., Einarsson, J., and Shaqfeh, E.S.G. (2020). Lift and drag force on a spherical particle in a viscoelastic shear flow. J. Nonnewton. Fluid Mech. *280*, 104279.

33. Pak, O.S., Zhu, L., Brandt, L., and Lauga, E. (2012). Micropropulsion and microrheology in complex fluids via symmetry breaking. Phys. Fluids *24*, 103102.

34. Su, Y., Castillo, A., Shun Pak, O., Zhu, L., and Zenit, R. (2022). Viscoelastic levitation. J. Fluid Mech. *943*, A23.

35. Kroo, L.A., Binagia, J.P., Eckman, N., Prakash, M., and Shaqfeh, E.S.G. (2022). A freely suspended robotic swimmer propelled by viscoelastic normal stresses. J. Fluid Mech. *944*, A20.

36. Gagnon, D.A., Keim, N.C., Shen, X., and Arratia, P.E. (2014). Fluid-induced propulsion of rigid particles in wormlike micellar solutions. Phys. Fluids *26*, 103101.

37. Bird, R.B., Armstrong, R.C., and Hassager, O. (1987). Dynamics of Polymeric Liquids. Vol. 1: Fluid Mechanics (John Wiley and Sons Inc.).

38. Larson, R.G. (2013). Constitutive Equations for Polymer Melts and Solutions: Butterworths Series in Chemical Engineering (Butterworth-Heinemann).

39. Morozov, A., and Spagnolie, S.E. (2015). Introduction to complex fluids. In Complex Fluids in Biological Systems: Experiment, Theory, and Computation, S.E. Spagnolie, ed. (Springer New York), pp. 3–52.

40. Apostolakis, M.V., Mavrantzas, V.G., and Beris, A.N. (2002). Stress gradient-induced migration effects in the Taylor–Couette flow of a dilute polymer solution. J. Nonnewton. Fluid Mech. *102*, 409–445.

41. Masoud, H., and Stone, H.A. (2019). The reciprocal theorem in fluid dynamics and transport phenomena. J. Fluid Mech. *879*, P1.

42. Aubert, J.H., and Tirrell, M. (1980). Macromolecules in nonhomogeneous velocity gradient fields. J. Chem. Phys. *72*, 2694–2701.

43. Aubert, J.H., Prager, S., and Tirrell, M. (1980). Macromolecules in nonhomogeneous velocity gradient fields. II. J. Chem. Phys. *73*, 4103–4112.

44. Helfand, E., and Fredrickson, G.H. (1989). Large fluctuations in polymer solutions under shear. Phys. Rev. Lett. *62*, 2468–2471.

45. Doi, M. (1990). Effects of viscoelasticity on polymer diffusion. In Dynamics and Patterns in Complex Fluids: New Aspects of the Physics-Chemistry Interface (Springer), pp. 100–112.

46. Milner, S.T. (1991). Hydrodynamics of semidilute polymer solutions. Phys. Rev. Lett. *66*, 1477–1480.

47. Mavrantzas, V.G., and Beris, A.N. (1992). Modeling of the rheology and flow-induced concentration changes in polymer solutions. Phys. Rev. Lett. *69*, 273–276.

48. Tsouka, S., Dimakopoulos, Y., Mavrantzas, V., and Tsamopoulos, J. (2014). Stress-gradient induced migration of polymers in corrugated channels. J. Rheol. *58*, 911–947.

49. Gomez-Solano, J.R., and Bechinger, C. (2015). Transient dynamics of a colloidal particle driven through a viscoelastic fluid. New J. Phys. *17*, 103032.

50. Kadoma, I.A., and van Egmond, J.W. (1997). Shear-enhanced orientation and concentration fluctuations in wormlike micelles: Effect of salt. Langmuir *13*, 4551–4561.

51. Ganapathy, R., and Sood, A.K. (2006). Intermittency route to rheochaos in wormlike micelles with flow-concentration coupling. Phys. Rev. Lett. *96*, 108301.

52. Teran, J., Fauci, L., and Shelley, M. (2010). Viscoelastic fluid response can increase the speed and efficiency of a free swimmer. Phys. Rev. Lett. *104*, 038101.

53. Liu, B., Powers, T.R., and Breuer, K.S. (2011). Force-free swimming of a model helical flagellum in viscoelastic fluids. Proc. Natl. Acad. Sci. USA *108*, 19516–19520.

54. Datt, C., and Elfring, G.J. (2019). Active particles in viscosity gradients. Phys. Rev. Lett. *123*, 158006.

55. Liebchen, B., Monderkamp, P., Ten Hagen, B., and Löwen, H. (2018). Viscotaxis: Microswimmer navigation in viscosity gradients. Phys. Rev. Lett. *120*, 208002.

56. Zöttl, A., and Yeomans, J.M. (2019). Enhanced bacterial swimming speeds in macromolecular polymer solutions. Nat. Phys. *15*, 554–558.

57. Dandekar, R., and Ardekani, A.M. (2020). Swimming sheet in a viscosity-stratified fluid. J. Fluid Mech. *895*, R2.

58. Shaik, V.A., and Elfring, G.J. (2021). Hydrodynamics of active particles in viscosity gradients. Phys. Rev. Fluids *6*, 103103.

59. Esparza López, C., Gonzalez-Gutierrez, J., Solorio-Ordaz, F., Lauga, E., and Zenit, R. (2021). Dynamics of a helical swimmer crossing viscosity gradients. Phys. Rev. Fluids *6*, 083102.

60. Stehnach, M.R., Waisbord, N., Walkama, D.M., and Guasto, J.S. (2021). Viscophobic turning dictates microalgae transport in viscosity gradients. Nat. Phys. *17*, 926–930.

61. Olsen, K.S., Angheluta, L., and Flekkøy, E.G. (2021). Active Brownian particles moving through disordered landscapes. Soft Matter *17*, 2151–2157.

62. De Corato, M., and Martínez-Lera, P. (2025). Enhanced rotational diffusion and spontaneous rotation of an active Janus disk in a complex fluid. Soft Matter *21*, 186–197.

Please cite this article in press as: De Corato et al., Colloidal Magnus effect in polymer solutions, Newton (2025), https://doi.org/10.1016/j.newton.2025.100373



63. Squires, T.M., and Brady, J.F. (2005). A simple paradigm for active and nonlinear microrheology. Phys. Fluids *17*, 073101.

64. Khan, M., Regan, K., and Robertson-Anderson, R.M. (2019). Optical tweezers microrheology maps the dynamics of strain-induced local inhomogeneities in entangled polymers. Phys. Rev. Lett. *123*, 038001.

65. Zöttl, A., and Yeomans, J.M. (2019). Driven spheres, ellipsoids and rods in explicitly modeled polymer solutions. J. Phys. Condens. Matter *31*, 234001.

66. Nitsche, L.C., and Hinch, E.J. (1997). Shear-induced lateral migration of brownian rigid rods in parabolic channel flow. J. Fluid Mech. *332*, 1–21.

67. Morris, J.F., and Boulay, F. (1999). Curvilinear flows of noncolloidal suspensions: The role of normal stresses. J. Rheol. *43*, 1213–1237.

68. Patteson, A.E., Gopinath, A., and Arratia, P.E. (2016). Active colloids in complex fluids. Curr. Opin. Colloid Interface Sci. *21*, 86–96.

69. Spagnolie, S.E., and Underhill, P.T. (2023). Swimming in complex fluids. Annu. Rev. Condens. Matter Phys. *14*, 381–415.

70. Wu, Z., Chen, Y., Mukasa, D., Pak, O.S., and Gao, W. (2020). Medical micro/nanorobots in complex media. Chem. Soc. Rev. *49*, 8088–8112.

71. De Corato, M., Greco, F., and Maffettone, P.L. (2015). Locomotion of a microorganism in weakly viscoelastic liquids. Phys. Rev. E *92*, 053008.

72. Villone, M.M., Hulsen, M.A., Anderson, P.D., and Maffettone, P.L. (2014). Simulations of deformable systems in fluids under shear flow using an arbitrary Lagrangian Eulerian technique. Comput. Fluids *90*, 88–100.